

2.2-2.4 Superconducting qubits

This lecture will be based on references [1], [2], [3], [4].

0 Introduction

In this lecture we will introduce all superconducting qubits. We will begin with the initial superconducting qubit, the Cooper pair box, that later evolved into the transmon qubit, the most widely used and known superconducting qubit. Then we will cover flux-like qubits starting with the rf-SQUID qubit used by DWave and then the persistent current flux qubit and the fluxonium qubit. Finally we'll introduce the qubits based in nonclassical states of harmonic oscillators in superconducting cavities.

1 The charge qubit

Discrete charge tunneling in normal metal and superconductors was a busy field of study in the 1980s and 1990s. Towards the end of the '90s, experiments found the first proof that coherent oscillations could be observed between two states different by a small amount of charge, a single Cooper pair.

1.1 The Cooper Pair Box Hamiltonian

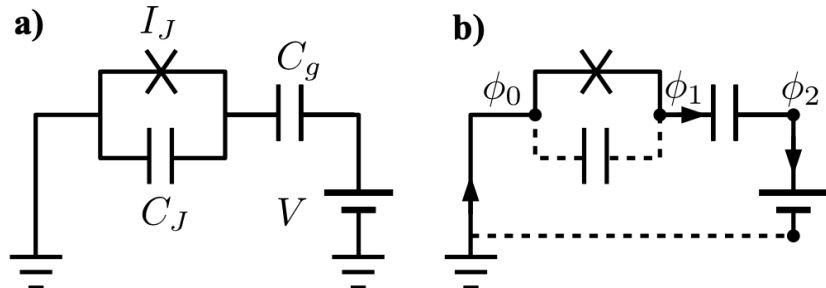


Figure 1: Circuit equivalent of the Cooper pair box charge qubit. From [1].

The Cooper Pair Box (CPB) circuit is shown in Fig. 1, which is basically the voltage-biased oscillator with the linear inductor replaced by the Josephson junction. Recovering the current conservation at node with flux Φ_1 ,

$$C\ddot{\Phi}_1 + I_C \sin(2\pi\Phi_1/\Phi_0) = C_g(\dot{V} - \ddot{\Phi}_1). \quad (1)$$

Re-writing it in the Euler-Lagrange form,

$$\frac{d}{dt} \left[C_\Sigma \left(\dot{\Phi}_1 - \frac{C_g}{C_\Sigma} \dot{V} \right) \right] = -I_C \sin(2\pi\Phi_1/\Phi_0), \quad (2)$$

with $C_\Sigma = C + C_g$. This leads to the Lagrangian

$$\mathcal{L} = \frac{1}{2} C_\Sigma \dot{\Phi}_1^2 - C_g \dot{\Phi}_1 V + E_J \cos(2\pi\Phi_1/\Phi_0). \quad (3)$$

$E_J = I_C \Phi_1 / 2\pi$. Applying the Legendre transformation brings us to the CPB Hamiltonian

$$\mathcal{H} = \frac{1}{2C_\Sigma} (q - q_g)^2 - E_J \cos(2\pi\Phi_1/\Phi_0), \quad (4)$$

where the external potential introduces the equilibrium charge $q_g = -C_g V$. The first term corresponds to the electrostatic energy of the island

$$E_{\text{el}} = \frac{1}{2C_\Sigma} (q - q_g)^2. \quad (5)$$

the second term being the Josephson energy with amplitude E_J .

1.2 The charge qubit Hamiltonian

With the Hamiltonian of the CPB obtained, we first quantize it and elevate the charge and flux variables into operators, $\{q, \Phi\} \rightarrow \{\hat{q}, \hat{\Phi}\}$. We can then project these operators in the charge basis $|n\rangle$.

The charge operator is diagonal in this basis $\hat{q}|n\rangle = -2en|n\rangle$. In the CPB, $|n\rangle$ represents the number of charges on the island. Using the charge number operator, $\hat{n} = \hat{q}/(-2e)$, the electrostatic energy is

$$\hat{E}_{\text{el}} = \frac{4e^2}{2C_\Sigma} (\hat{n} - n_g)^2 = 4E_C(\hat{n} - n_g)^2, \quad (6)$$

where we defined two important quantities. The first is the charging energy $E_C = e^2/2C_\Sigma$, corresponding to the addition of a single electron charge on the island. The second is the gate charge, $n_g = C_g V / 2e$, induced by the external voltage V . Let's calculate the electrostatic energy of n Cooper pairs on the island,

$$\hat{E}_{\text{el}}|n\rangle = 4E_C(n - n_g)^2|n\rangle. \quad (7)$$

Setting n_g , notice the energy difference between having n and $n+1$, or $n+2$ charges, being $4E_C(2n+1)$ or $4E_C(4n+4)$, respectively. This clearly displays a quite anharmonic spectrum. We can plot different parabolas as function of gate

charge n_g corresponding to different number of charges n , $n + 1$, etc. (see dashed lines on Fig. 2). Notice that the parabolas corresponding to n and $n + 1$ cross at $n_g = \pm 1/2$, therefore becoming degenerate and far away from other states with higher n . These areas will become very relevant to consider the charge qubit. If we just restrict ourselves to these two states, the charging energy can only take two values separated by an energy $\hbar\varepsilon = 8E_C(n_g - 1/2)$. We can use the Pauli matrix representation to express this energy as $(\hbar\varepsilon/2)\hat{\sigma}_z$, where $\hat{\sigma}_z \equiv |n+1\rangle\langle n+1| - |n\rangle\langle n|$ is a longitudinal qubit operator.

Now let's consider the second term, the Josephson energy. We recall that its representation in the charge basis is quite simple,

$$-E_J \cos(2\pi\hat{\Phi}/\Phi_0) = -\frac{E_J}{2} \sum_n (|n\rangle\langle n+1| + |n+1\rangle\langle n|). \quad (8)$$

In the regime of the charge qubit, where we are fixing the value of the charges to states $|n\rangle$ and $|n+1\rangle$, this operator can also be expressed as a transverse Pauli matrix $\hat{\sigma}_x \equiv |n+1\rangle\langle n| + |n\rangle\langle n+1|$. Therefore, we can rewrite the Cooper pair Hamiltonian as a 2×2 matrix

$$\hat{H} = \frac{\hbar\varepsilon}{2}\hat{\sigma}_z - \frac{\hbar\Delta}{2}\hat{\sigma}_x, \quad (9)$$

with $\hbar\Delta = E_J$ the tunneling energy amplitude. The full energy spectrum of the CPB is shown in Fig. 2. By replacing the junction with a symmetric DC-SQUID, we obtain a flux-tunable Josephson energy,

$$E_J(\Phi) \equiv (\Phi_0/2\pi)2I_C|\cos(\pi\Phi/\Phi_0)|. \quad (10)$$

This allows adjusting the tunneling amplitude $\Delta(\Phi)$ with an external knob. The electrostatic energy can be tuned by adjusting the gate voltage V which sets the gate charge n_g . We have a fully tunable qubit Hamiltonian. We will see later that the tunability in the charge also presents a big problem since charge noise is unbearable in current experiments.

We have seen that obtaining this simplified expression is possible in the regime where the number of charges is well defined. In other words, where the charge number is a good quantum number of the charge operator \hat{q} . This is the regime where the charging energy term with amplitude E_C dominates over the Josephson energy term with amplitude E_J . Typically in experiments $E_J/E_C = 0.1 - 1$ for charge qubits.

The qubit Hamiltonian can be readily diagonalized to be written as $H/\hbar = -(\omega_q/2)\hat{\sigma}'_z$, with a Pauli matrix operator $\hat{\sigma}'_z$ expressed in the diagonal basis of the qubit $\hat{\sigma}'_z = |e\rangle\langle e| - |g\rangle\langle g|$. The energy of the qubit is therefore

$$\hbar\omega_q = \hbar\sqrt{\varepsilon^2 + \Delta^2}. \quad (11)$$

This defines a hyperbola. The ground/excited states have therefore energy $E_{e/g} = \pm(1/2)\omega_q$. The states in the diagonal basis can be expressed as function of the non-diagonal basis (sometimes referred to as logical basis, laboratory basis, or, in this

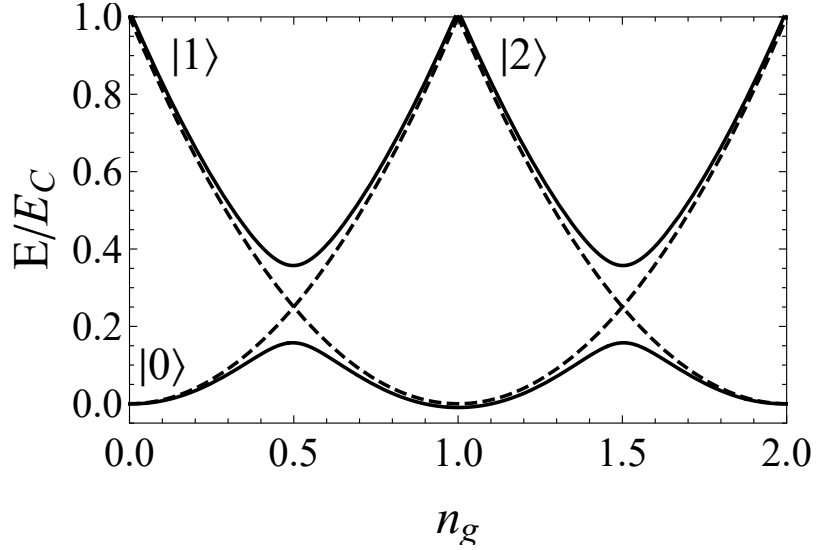


Figure 2: Energy levels (solid line) of the CPB as function of the gate charge n_g . Dashed lines represent only the charging energy states without Josephson tunneling. From [1].

case, charge basis):

$$|g\rangle = \cos(\theta/2)|0\rangle - \sin(\theta/2)|1\rangle, \quad (12)$$

$$|e\rangle = \sin(\theta/2)|0\rangle + \cos(\theta/2)|1\rangle. \quad (13)$$

Here, $\sin \theta \equiv \Delta/\omega_q$, $\cos \theta = \varepsilon/\omega_q$. The qubit hyperbola is symmetric with respect to the symmetry point, $\varepsilon = 0$, where the qubit gap is minimal and is given by $\omega_q = \Delta$. Clearly, the finite tunneling leads to a breaking of the degeneracy of states with n and $n+1$ charges as $n_g = 1/2$. At this point, the eigenstates become superpositions of charge states:

$$|\pm\rangle = \frac{|0\rangle \pm |1\rangle}{\sqrt{2}}. \quad (14)$$

Far away from the symmetry point, $\varepsilon \gg \Delta$, the states become pure charge states

$$|g\rangle = |0\rangle, \quad (15)$$

$$|e\rangle = |1\rangle, \quad (16)$$

and the energy of the states is given by $E_{0,1} \simeq \pm \varepsilon/2$.

The symmetry point $\varepsilon = 0$ is very relevant experimentally, as at this point the qubit energy is to first order insensitive to the gate charge, $\partial\omega_q/\partial\varepsilon = 0$, which means the qubit experiences no dephasing due to charges at this point. Stray charges will induce fluctuations in the voltage of the island δV , leading to fluctuations in ε and thus in the qubit splitting.

The term ε may contain both a static component ε_0 as well as a dynamic component $\varepsilon(t)$, $\varepsilon = \varepsilon_0 + \varepsilon(t)$. This time-domain part is the way to drive transitions in the qubit. Going back to Eq. (4), the cross term $\hat{q}q_g/C_\Sigma$ represents the dipole coupling $\hat{U}_d = \hat{\mathbf{d}} \cdot \hat{\mathbf{E}}(t)$ between the qubit electric dipole moment operator $\hat{\mathbf{d}} \equiv -2e\hat{n}$ and the

external field operator $\hat{\mathbf{E}}(t) \equiv (C_g/C_\Sigma)\hat{V}(t)$. The form of $\hat{V}(t)$ will be discussed in the next chapter on qubit control. Writing out the time-dependent term explicitly results in the qubit Hamiltonian

$$\hat{H} = \frac{\hbar\varepsilon_0}{2}\hat{\sigma}_z - \frac{\hbar\Delta}{2}\hat{\sigma}_x - 2e\frac{C_g}{C_\Sigma}V(t)\hat{\sigma}_z. \quad (17)$$

The last term of this Hamiltonian is the electric dipole coupling between the qubit electric dipole $\hat{\mathbf{d}}_e \equiv -2e\hat{n}$, and an external field generating the voltage $V(t)$. In the charge degeneracy $\varepsilon_0 = 0$,

$$\hat{H} = -\frac{\hbar\Delta}{2}\hat{\sigma}_z - e\frac{C_g}{C_\Sigma}V(t)\hat{\sigma}_x. \quad (18)$$

Here, we have rotated the basis by 90° in the \hat{y} axis. It is clear from this expression that the matrix dipole element of the dipole operator, $\langle i|\hat{\mathbf{d}}_e|j\rangle$ is 0 for diagonal elements, $\langle e|(-2e\hat{\sigma}_x)|e\rangle = \langle g|(-2e\hat{\sigma}_x)|g\rangle = 0$, while for off-diagonal elements its value is $|\langle 0|\hat{d}_e|1\rangle| = |\langle 1|\hat{d}_e|0\rangle| = 2e$. This will be useful when representing external fields being applied to the qubit to drive transitions.

As the charge qubit eigenstates contain a well-defined number of charges n (even at the symmetry point where the average is zero $\langle n \rangle = 0$), a method to detect the qubit state is to directly measure the charge on the island with a charge sensor. As an example, one may use a single-electron transistor (known as SET) [].

1.3 Experimental implementation

The Cooper pair box, or charge qubit, was the first-ever superconducting qubit to be implemented experimentally. In 1999, a team led by Prof. Y. Nakamura at NEC observed the first coherent oscillations of charge states in a small superconducting island connected to a big superconducting reservoir via a Josephson junction [5] (Fig. 3). Despite the great success, the qubit was short lived, with just a few nanoseconds of lifetime. Charge noise was just overwhelming the device.

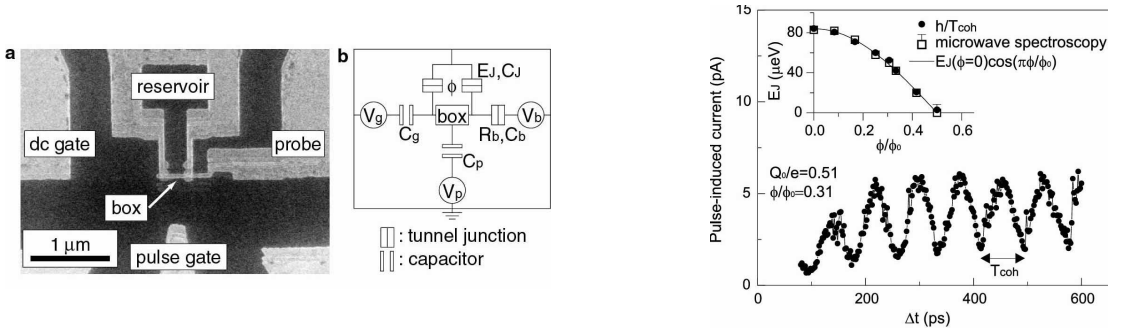


Figure 3: (Left) Original Cooper Pair Box circuit used at NEC. (Right) Rabi oscillations of the CPB at NEC. From [5].

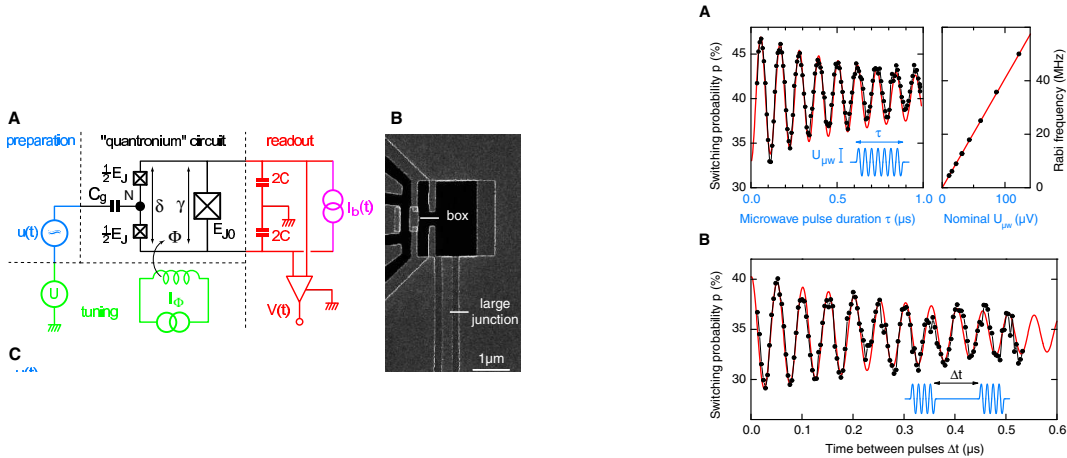


Figure 4: (Left) Quantronium circuit used at Saclay. (Right) Rabi oscillations and Ramsey fringes of the quantronium qubit. From [6].

Follow-up experiments in 2002 showed improvements, particularly in the group of CEA Saclay in Paris with the modified CPB circuit known as Quantronium (Fig. 4), a record-high coherence time above 1 microsecond was observed [6].

Shortly after, in 2003, two-qubit experiments at NEC showed coherent oscillations between the two qubits [7], followed by a controlled-NOT operation [8]. In a parallel development, the Yale group introduced the concept of circuit QED by embedding the qubit inside a resonator structure [9, 10]. This way, the qubit is only exposed to the resonator modes, which acts like a filter for the qubit (we will see this in the following chapter of this course).

In all the experiments, the Josephson to charge energy ratio, E_J/E_C was always near 1, which we identify as the purely charging regime where the charge number operator \hat{n} is a good quantum number, and charge number states $|n\rangle$ properly describe the quantum state of the circuit.

But the reality with the Cooper pair box was evident from noise characterization, as found in Refs. [11, 12], where it was found that high frequency qubit noise came from vacuum fluctuations of the impedance of the measurement and control circuit, while low frequency noise was coming from $1/f$ charge noise (Fig. 5).

These findings of the large extent of the impact of charge noise rendered the charge qubit ineligible for large-scale quantum processors. It was not until 2007 when the Yale group found a way to turn the circuit insensitive to charges, in a circuit known as the transmon qubit, to be studied in the following section.

2 The transmon qubit

With little hope for the charge qubit, the Yale group in 2007 came with a revolutionary idea that changed the field of superconducting qubits by creating the simplest

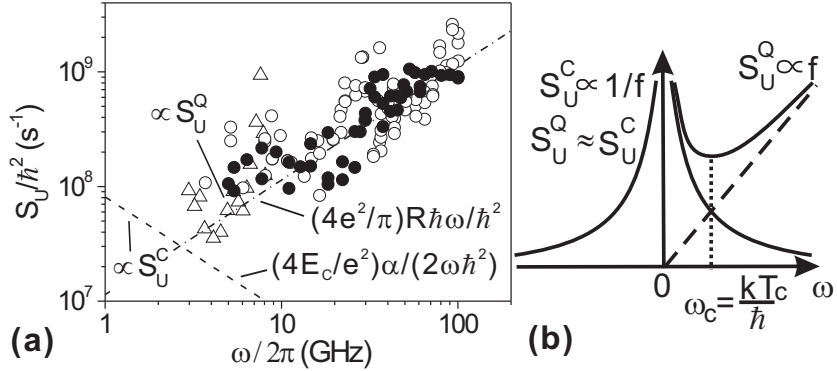


Figure 5: Charge noise spectrum in a CPB, showing an amplitude of $1/f$ noise of $(1.3 \times 10^{-3}e)^2$, which turns out too high to operate the qubit reliably. From [11].

and functional qubit: the transmon qubit [3]. The key idea was to reduce the sensitivity to background charges experienced by the CPB qubit. This was achieved by increasing the E_J/E_C ratio to large values, close to 100, which is in fact the regime of flux qubits (seen in next section).

In the phase representation, the CPB Hamiltonian becomes

$$H_{\text{CPB}} = 4E_C \left(-i \frac{\partial}{\partial \varphi} - n_g \right)^2 - E_J \cos \varphi. \quad (19)$$

This equation can be solved analytically, leading to the Mathieu functions. The energy level spectrum can be plotted as function of the E_J/E_C ratio, as seen in Fig. 6. The charge dispersion is dramatically reduced for exceeding values of E_J/E_C [3].

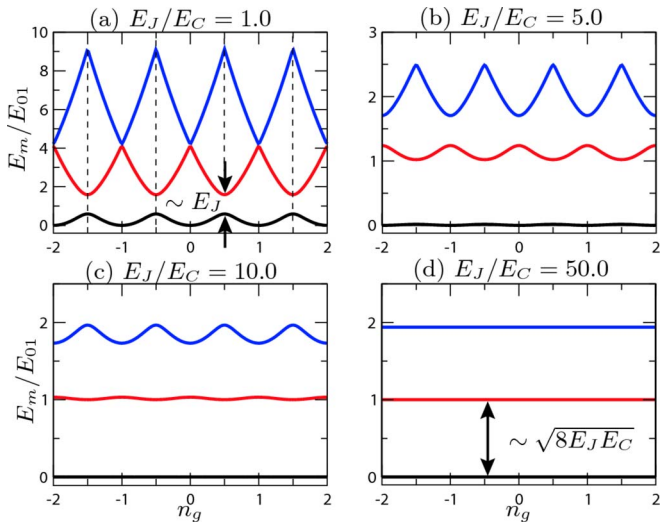


Figure 6: Energy level spectrum of the CPB with increasing E_J/E_C ratio. From [3].

For large E_J/E_C , the CPB energy level splitting away from the charge degeneracy point can be approximated in a tight-binding model

$$E_m(n_g) \simeq E_m(n_g = 1/4) - \frac{\epsilon_m}{2} \cos(2\pi n_g), \quad (20)$$

where $\epsilon_m \equiv E_m(n_g = 1/2) - E_m(n_g = 0)$ is the peak-to-peak charge dispersion of level m . The analytic form from the Mathieu solution is [3] shows $\epsilon_m \sim \exp(-\sqrt{8E_J/E_C})$, which means that for increasing E_J/E_C ratio the charge dispersion is exponentially suppressed. This can be seen in Fig. 7. Therefore, we need to

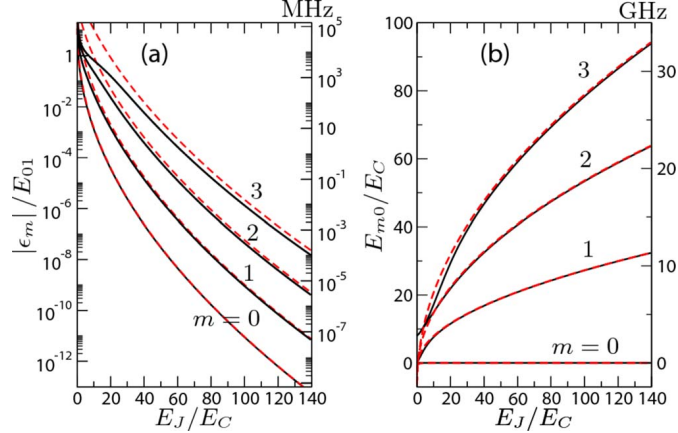


Figure 7: (a) Comparison of charge dispersion as function of E_J/E_C . (b) Energy level difference as function of E_J/E_C . All plots are calculated at $n_g = 1/2$ and assuming $E_C/h = 0.35$ GHz. From [3].

move in this direction to avoid charge dependence. This is in practice achieved by adding a large capacitor in parallel to the Josephson junction connection to island to ground, as seen in Fig. 8. This large capacitor results in an increased total capacitance for the superconducting island of $C_\Sigma = C_B + C_J$, where C_B is the shunting capacitance. This reduces the charging energy significantly $E_C = e^2/2C_\Sigma$.

The consequence of entering the large E_J/E_C regime is that now the potential is deep and it contains multiple energy bands, which no longer represent states with a finite charge. In other words, the system is locked near the bottom of the cosine potential of the Josephson junction. The potential energy is shown in Fig. 9. The chance for the system to tunnel outside the potential well is exponentially suppressed by the barrier height $\sim E_J$.

2.1 The transmon Hamiltonian

In the regime $E_J/E_C \gg 1$, the charge number operator will not be well defined, therefore the phase is a better quantum number. So technically, we no longer have a charge qubit. Rather, it is a nonlinear oscillator. We may now use the fact that the phase will stay around 0, and expand the cosine potential, to yield the transmon Hamiltonian

$$\mathcal{H}_{\text{tr}} \simeq \frac{1}{2C_\Sigma}(\hat{q} - q_g)^2 - E_J + \frac{E_J}{2\varphi_0^2}\hat{\Phi}^2 - \frac{E_J}{24\varphi_0^4}\hat{\Phi}^4 + \mathcal{O}(\hat{\Phi}^6). \quad (21)$$

This is the Hamiltonian of an LC oscillator with a quartic nonlinear term. The plasma frequency of this oscillator is $\hbar\omega_p \simeq \sqrt{8E_C E_J}$. Taking just the quadratic

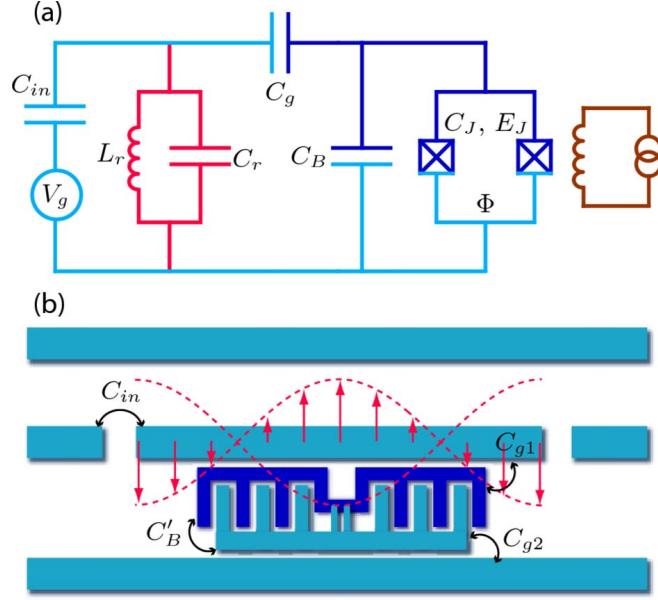


Figure 8: (a) Circuit schematic of the transmon qubit, including its readout resonator. (b) Sketch of the real geometric shape of a transmon qubit coupled to a CPW resonator. From [3].

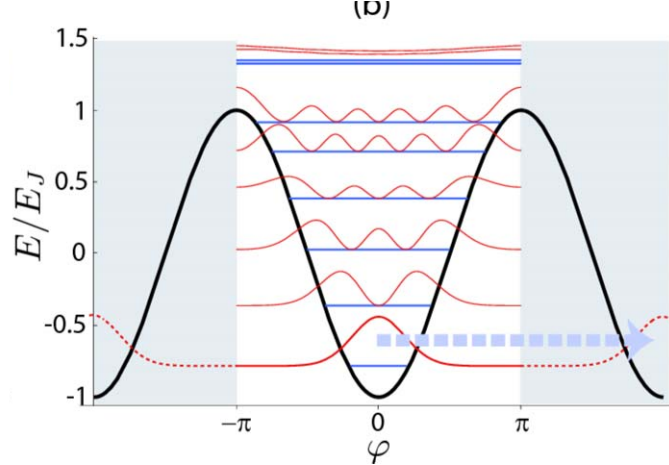


Figure 9: Potential energy of the transmon qubit with several levels inside it. From [3].

terms, we can use creation and annihilation operators as

$$\hat{q} = -2e\hat{n} = 2e \left(\frac{E_J}{8E_C} \right)^{1/4} \frac{i}{\sqrt{2}} (\hat{a}^\dagger - \hat{a}), \quad (22)$$

$$\hat{\Phi} = \varphi_0 \left(\frac{8E_C}{E_J} \right)^{1/4} \frac{1}{\sqrt{2}} (\hat{a}^\dagger - \hat{a}). \quad (23)$$

With these operators and up to second order in perturbation theory, the Hamiltonian becomes

$$\mathcal{H}_{tr} \simeq \hbar\omega_p \hat{a}^\dagger \hat{a} - \hbar\alpha \hat{a}^\dagger \hat{a}^\dagger \hat{a} \hat{a} + i\hbar\varepsilon(\hat{a}^\dagger + \hat{a}). \quad (24)$$

The last term is the external field $q_g \hat{q}/C_\Sigma$. We also defined the quantity

$$\alpha \equiv \omega_{12} - \omega_{01}, \quad (25)$$

which is the so-called anharmonicity, which for the transmon verifies $\alpha/\omega_{01} \ll 1$. This small anharmonicity is the price to pay for reducing the charge dispersion, as can already be seen in Fig. 7(b). Using the exact expression of the wavefunctions, the energy level E_m has energy

$$E_m \simeq -E_J + \sqrt{8E_J E_C} \left(m + \frac{1}{2} \right) - \frac{E_C}{12} (6m^2 + 6m + 3). \quad (26)$$

With this expression, the anharmonicity in the transmon regime becomes $\alpha \simeq -E_C$. A plot of α as function of E_J/E_C is shown in Fig. 10. Typically in real experiments, the anharmonicity is in the 3-5% range of the transition frequency ω_{01} . This means ~ 300 MHz for a ~ 6 GHz transition. The reduced anharmonicity has the negative consequence of smaller addressability. That is, when driving the transition $0 \rightarrow 1$, there is a finite probability of driving the transition $1 \rightarrow 2$ off-resonantly. This is a source of gate errors and leakage outside the qubit subspace. Several methods have already been implemented, such as the DRAG scheme [13].

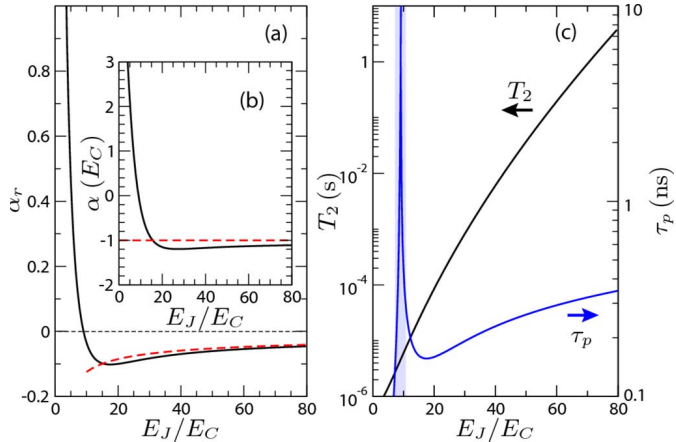


Figure 10: (a) Relative $\alpha_r = \alpha/\hbar\omega_{01}$ and (b) absolute α values of the anharmonicity of the transmon as function of E_J/E_C , at $n_g = 1/2$. (c) Estimated dephasing time T_2 from charge fluctuations, and minimum pulse duration τ_p to avoid populating other states. From [3].

Similarly to the Cooper Pair Box charge qubit, using the form of the charge operator in Eq. (22), the electric dipole operator for the transmon $\hat{\mathbf{d}}_{\text{tr}}$ which appears in the term proportional to ε in the Hamiltonian becomes for the transmon

$$\hat{\mathbf{d}}_{\text{tr}} \equiv |\langle 0|2e\hat{n}|1\rangle|(\hat{a}^\dagger - \hat{a}) = \sqrt{2}e \left(\frac{E_J}{8E_C} \right)^{1/4} (\hat{a}^\dagger - \hat{a}). \quad (27)$$

This operator will also have off-diagonal elements that will drive transitions to the transmon, even when they cannot change the energy of the system. Compare this to the electric dipole moment of the Cooper Pair box, which was simply $2e$.

If the external drive applied to the transmon is well behaved, we can consider the transmon to lie in its two lowest states and hence represent it as a two-level system:

$$H_{\text{tr}} = \frac{1}{2}\hbar\omega_{01}\sigma_z + \hbar\varepsilon\sigma_y. \quad (28)$$

If we replace the transmon junction with a DC-SQUID, then applying a magnetic flux Φ allows us to tune $E_J(\Phi)$ and therefore the energy level splitting $\omega_{01}(\Phi) = \omega_{01}(0)\sqrt{\cos(\pi\Phi/\Phi_0)}$. The transmon is therefore a fully controllable qubit.

2.2 Experimental implementation

The first transmon qubits were developed at Yale University in the US at the group of Prof. Robert Schoelkopf and Prof. Michel Devoret [3]. They immediately showed a dramatic increase of the qubit coherence properties to lie in the few-microsecond timescale, as compared to the sub-microsecond exhibited by the Cooper pair box [14]. This allowed that group to take the lead and begin operating two-qubit devices and observing coherent oscillations between them [15], as well as using the qubit to detect arbitrary photon states in the resonator by reaching a new regime in light-matter interactions known as the strong dispersive regime [16]. Eventually the Yale group managed to be the first one to implement a quantum algorithm in a 2-qubit superconducting device, the Deutsch-Josza and the Grover algorithm [17].

The real power of the transmon lies in its simplicity. It is this reason that made so many other groups begin employing transmon qubits. In this way, the Wallraff group at ETH Zurich began operating in 2007 fully with transmon qubits [18]. Other groups, such as the one in Saclay, also started to incorporate transmon qubits in their experiments, phasing out the quantronium qubit [19].

But despite the success with the transmon, the progress in improving the qubit coherence properties seemed to stall for some years. It was not until 2011 when again the Yale group made a new breakthrough by enclosing a transmon qubit inside a 3D cavity made of aluminum, displaying strong coupling to the cavity modes [20]. The most remarkable was more than an order of magnitude in increase of both T_1 and T_2 , the reason being the massive size of the transmon (capacitor plates in the mm^2 range), which reduced the electric field intensity, thus reducing the interaction to surface defects. This discovery impacted back on the planar circuit geometry, leading to larger capacitor plates and better coherence times. By this time, a revolution started in the field with many new groups starting, most of them using transmons. This included large companies like IBM and Google. This kicked off the industry race to build a quantum computer.

Prior to the appearance of Google, the UCSB group led by Prof. John Martinis had managed to significantly improve the planar transmon properties to large levels, by introducing their X-mon geometry, where one capacitor plate is a cross and the ground plane is the rest of the capacitor. This design led to tens of microseconds T_1 and T_2 [21]. The Google group took the lead in scaling up their transmon system, being the first group to reach 5 qubits [22], 9 qubits with error detection [23], digital simulation of the adiabatic algorithm [24] and eventually the 54-qubit that attained the quantum supremacy [25].

The transmon qubit keep being the workforce superconducting qubit in the world, with new materials, new geometries, new applications.

3 The flux qubit

Now we enter a new family of superconducting qubits: the flux-based qubits. These qubits are qualitatively distinct from the Cooper pair box and the transmon in which their eigenstates can be modified by the presence of an external magnetic field. Therefore, these type of qubits consist of at least a superconducting loop threaded by a flux. The eigenstates correspond to charge flowing in the enclosed loop.

The particularities of the eigenstates of flux-like qubits are explained by the frustration of currents. Fluxoid quantization imposes that the total phase around the loop must satisfy $\delta\phi_{\text{loop}} = N\Phi_0 + \Phi_{\text{ext}}$. When $\Phi_{\text{ext}} = \Phi_0/2$, there are two values of $\delta\phi = \pm\Phi_0/2$ that satisfy the fluxoid quantization, correponding to N and $N + 1$ fluxoids, respectively. Each of the two values of $\delta\phi$ represents current flowing either clockwise or counterclockwise.

3.1 The rf-SQUID as the basic flux qubit

All flux-qubit types boil down to a very basic design which is the one defined in an rf-SQUID circuit: a loop with inductance shunting a single Josephson junction, as shown in Fig. 11. This circuit is described by the following Hamiltonian (obtained

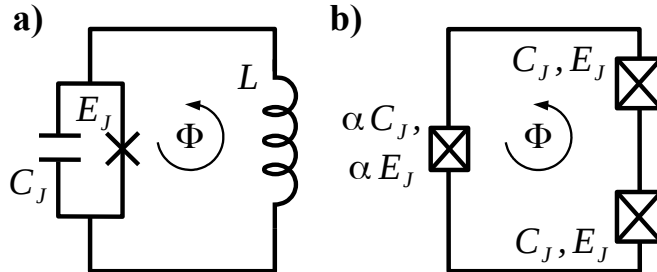


Figure 11: (a) rf-SQUID circuit. (b) Persistent current qubit circuit. From [1].

in the previous chapter on circuit quantization):

$$\hat{H} = \frac{1}{2C_J}\hat{q}^2 + \frac{1}{2L}\hat{\Phi}^2 - E_J \cos[2\pi(\hat{\Phi} + \Phi_{\text{ext}})/\Phi_0]. \quad (29)$$

This Hamiltonian can be interpreted as a particle in the potential defined by the cosine and parabolic terms. These terms interfere and create different scenarios depending on the externally applied flux Φ_{ext} . The presence of the capacitance tends to delocalize the wavefunction in each well of the potential energy. Since the qubit operates in the regime of $E_J/E_C \gg 1$, the potential energy already provides good intuition to the qubit dynamics.

Near $\Phi_{\text{ext}} = 0$, there is a single well with the lowest energy and the wave functions will resemble those of the anharmonic oscillator (transmon). Also, in this case $\langle \hat{\Phi} \rangle = 0$, similar to a transmon qubit.

Near $\Phi_{\text{ext}} = \Phi_0/2$ the system turns more interesting as there are two minima giving a finite net flux in each well $\langle \hat{\Phi} \rangle \neq 0$, i.e., we introduced frustration in the system. Due to tunneling over or through the intermediate barrier, the two wells hybridize, producing eigenstates that correspond to the superposition of the two minima in each well, states with a finite flux, or current, in the loop with opposite sign. The double-well scenario will take place only if $\beta = L_J/L = E_J/E_L < 1$.

To understand the quantum mechanics of the frustrated rf-SQUID, let's consider each well separately. If they are deep enough, the wave function in each well may be approximated as a harmonic oscillator, the wave function of which is a gaussian centered around the minima φ_L, φ_R of each of the two respective wells

$$\Psi_{L,R}(\varphi) = \langle \hat{\varphi} | L, R \rangle \sim \exp \left[-\frac{1}{2\sigma_\varphi^2} (\varphi - \varphi_{L,R})^2 \right]. \quad (30)$$

The wavefunctions of the left $|L\rangle$ and right $|R\rangle$ correspond to the left- and right-moving currents in the loop. The width $\sigma_\varphi \sim \sqrt{8E_C/E_J}$ is both the uncertainty of the phase variable and the spreading of the wavefunction.

At low temperatures, the qubit will be near the ground states $|L\rangle$ and $|R\rangle$. Therefore, we can project the whole Hamiltonian H onto the subspace spanned by these two states. Note that due to the spread of the wave function $\hbar t = \langle L|R \rangle \neq 0$. In other words, the tunneling rate t induces mixing between the two persistent current states. Also, if the system is not exactly at $\Phi_0/2$, the two wells will not be aligned to the same energy. Depending on the sign of extra flux $\delta\Phi$, the lowest well will be the left or right well. An offset energy will then exist between the two $\hbar\varepsilon = \mu \times \delta\Phi = (1/2)(\langle L|H|L \rangle - \langle R|H|R \rangle)$, where $\mu = I_p S$ is the magnetic dipole moment of the qubit given by the product of the persistent current I_p and the loop surface S . Thus we arrive at the two-level flux qubit reduced Hamiltonian

$$\hat{H} \simeq \mu \times \delta\Phi (|L\rangle\langle L| - |R\rangle\langle R|) + \hbar t (|R\rangle\langle L| + |L\rangle\langle R|). \quad (31)$$

Since $|L\rangle$ and $|R\rangle$ are not orthogonal, it is not the best set of states to be defined as a qubit. It is better to define the qubit states as $|0\rangle = (|L\rangle + |R\rangle)/\sqrt{2}$ and $|1\rangle = (|L\rangle - |R\rangle)/\sqrt{2}$. There is a freedom to choose which state is the ground state among the two superpositions, $(|L\rangle \pm |R\rangle)/\sqrt{2}$. This is due to the fact that we have truncated the full Hamiltonian in Eq. (29) down to the lowest 2 levels. When solving the eigenstates for the full circuit (see Fig. 14 below), it is seen that the ground state is the symmetric superposition $(|R\rangle + |L\rangle)/\sqrt{2}$. In this new basis, the Hamiltonian can be finally cast as

$$\hat{H} = \hbar\varepsilon\hat{\sigma}_z + \mu\delta\Phi\hat{\sigma}_x. \quad (32)$$

This Hamiltonian contains a fixed energy gap $\Delta = 2t$ at $\delta\Phi = 0$ that depends on the amount of tunneling t between wells, and an adjustable magnetic field bias energy $\hbar\varepsilon = \mu\delta\Phi$ that can be used to implement single-qubit operations.

Traditionally, the rf-SQUID has some drawbacks. It requires a large loop inductance to satisfy $L > L_J$ (see Fig. 12). Using just geometric inductance, this

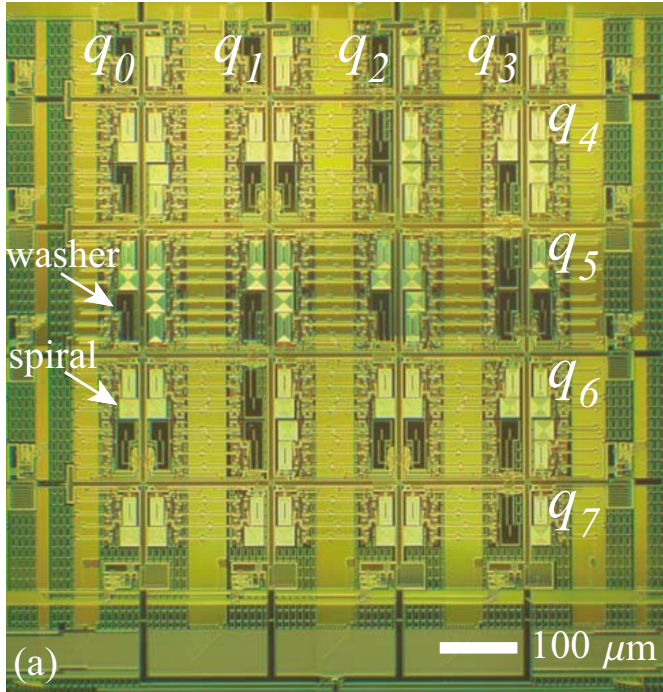


Figure 12: Array of rf-SQUID flux qubits coupled to each other in a 4×2 matrix used in the D-Wave quantum annealers. The qubits can be appreciated as the thin, long lines that cross defining a squared grid. From [26].

implies a very large loop. Large loops are susceptible to pick up more microscopic flux fluctuations, and therefore hinder qubit coherence. The additional drawback is the exponential dependence of the gap on the tunneling rate, which eventually is related to the junction dimensions, making t often uncontrollable. A solution to the first problem is to use Josephson junctions instead of geometric inductors to define the double-well potential, leading to the persistent current flux qubit in the next section. For the latter problem, a possible solution is to capacitively shunt the junction. We must add that recently superinductances have appeared that lead to small footprint rf-SQUIDs, bringing them back into the race to build quantum computers.

3.2 The Persistent Current (PC) flux qubit

The persistent current qubit, or simply flux qubit, was proposed in 1999 [27, 4] and first observed in 2000 [28]. As mentioned in the previous section, this qubit is an evolution from the rf-SQUID circuit where the linear inductor is replaced by a series of Josephson junctions that participate in forming the same double-well potential as in the rf-SQUID circuit.

The flux qubit circuit, in its simplest form [Fig. 11(b)], consists of 2 additional, larger Josephson junctions, with the smaller junction being a factor α smaller. An external flux threads the loop, and when this flux equals Φ_0 , the qubit finds itself in the same scenario of frustrated persistent currents. The main difference with the rf-SQUID is the loop size, being a few microns for the flux qubit and over 100 microns

for the rf-SQUID. This factor not only improves coherence times significantly, but also makes the footprint smaller for denser circuits. The two junctions, though, cannot simply be replaced by a linear inductance as their size is not large enough to neglect their nonlinear contribution to the qubit spectrum.

The circuit Hamiltonian is that of 3 Josephson junctions. The larger two are taken identical for simplicity.

$$\hat{H} = \frac{1}{2(1/2 + \alpha)} \hat{q}_+^2 + \frac{1}{2C_j} \hat{q}_-^2 + \alpha E_J \cos\left(\frac{\Phi_{\text{ext}} - \hat{\phi}_+}{2\varphi_0}\right) - 2E_J \cos(\hat{\phi}_+/2\varphi_0) \cos(\hat{\phi}_-/2\varphi_0). \quad (33)$$

Here we used $\phi_{\pm} = \phi_1 \pm \phi_2$, and fluxoid quantization $\phi_{\alpha} = \Phi_{\text{ext}} - \phi_+$. The resulting potential has 2 terms that interfere. The second term $\sim \cos(\phi_+/2\varphi_0)$ that favors $\phi_+ = \phi_- = 0$, and the first term which can be displaced by the external flux Φ_{ext} . Unfortunately, the Hamiltonian obtained here does not let itself be treated analytically and one needs to resort to numerics. The Hamiltonian can either be expressed in the flux or in the charge basis of states. For ease of computation, we tend to represent it in the charge basis, as the Josephson terms result in sparse matrices that turn out quite simple to diagonalize. Working in the charge basis requires introducing a cutoff in the number of states, as a flux-like qubit state isn't an eigenstate of the charge basis. Usually, a maximum of 9-10 Cooper pair number (both positive and negative) is sufficient to obtain a faithful representation of the qubit spectra and wave functions.

Fig. 13 shows the qubit potential for different flux values. Figures 13(a), (c), the flux at $\Phi_{\text{ext}} = 0$ shows a single well, leading to a potential close to that of a transmon. Then, Figs. 13(b), (d), at $\Phi_{\text{ext}} = \Phi_0/2$ show a double-well potential. Following numerical diagonalization, Fig. 13(e) displays the energy levels of the qubit as function of the external magnetic flux in the loop near the symmetry point for $\alpha = 0.7$. The lowest two states approach and define a two-level system well isolated from the higher-lying states. Figure 13(f) plots the energy differences, known as the spectrum, for increasing values of α . The decrease is given by the increase in the barrier between the two wells, lowering in this way the tunneling rate and the wave function overlap. Clearly, the qubit anharmonicity is gigantic when compared to the transmon case. This is because of the nature of the states, being related to wave function tunneling rather than a plasma oscillation. Being highly anharmonic, allows the qubit to be driven at ultrahigh speeds, even below a nanosecond [29].

The qubit wave functions are displayed in Figs. 14 and 15 for a large gap of 9 GHz and a smaller gap of 30 MHz, respectively. The wave function clearly appears as an overlap between the two gaussians in each well. The ground state is a symmetric superposition (an even wave function) and the excited state is an odd-parity superposition of the wave functions in each well. In the large-gap case, the energy levels lie above the potential barrier, while in the small gap they lie below. People often talk about macroscopic quantum tunneling in scenarios as in the low-gap case.

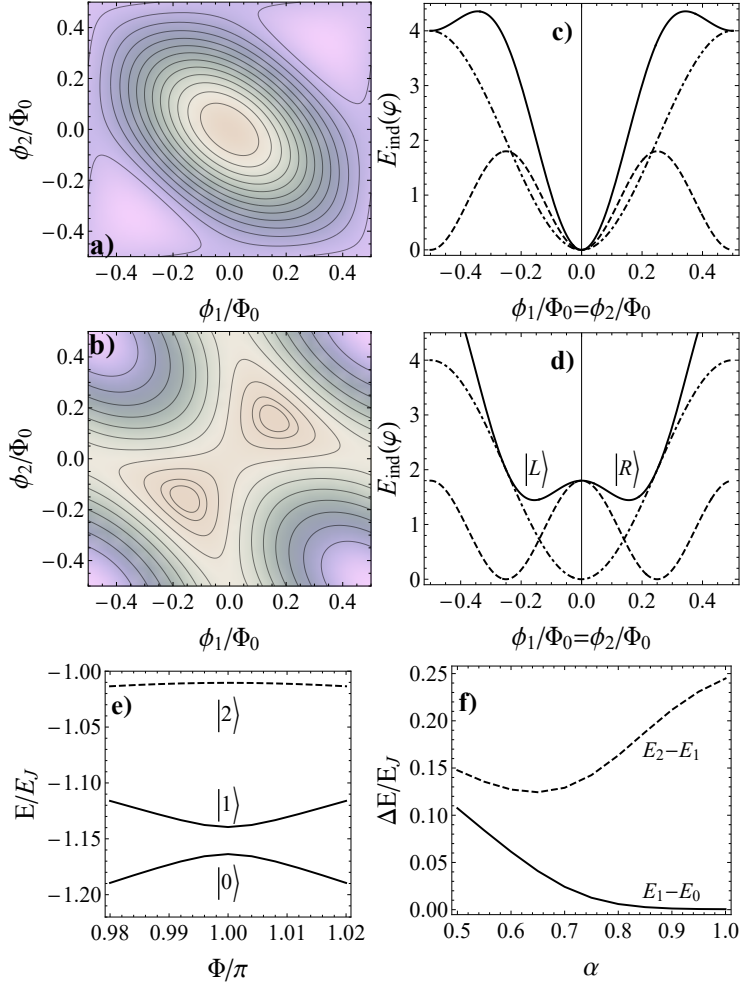


Figure 13: (a) Flux qubit potential at $\Phi_{\text{ext}} = 0$ and $\alpha = 0.9$. (b) (Solid line) Cross section of the potential along $\phi_1 = \phi_2$ for $\Phi_{\text{ext}} = 0$ and $\alpha = 0.9$. In dashed lines, the two cosine terms in the potential are plotted separately. Only a single minimum appears. (c) Flux qubit potential at $\Phi_{\text{ext}} = \Phi_0/2$ and $\alpha = 0.9$. (d) (Solid line) Cross section of the potential along $\phi_1 = \phi_2$ for $\Phi_{\text{ext}} = \Phi_0/2$ and $\alpha = 0.9$. In dashed lines, the two cosine terms in the potential are plotted separately. Only a single minimum appears. Two degenerate minima appear. (e) Energy levels from circuit near $\Phi_{\text{ext}} = \Phi_0/2$ for $\alpha = 0.7$. (f) Energy-level splitting at $\Phi_{\text{ext}} = \Phi_0/2$ as function of α . From [1].

We can still apply a two-state truncation of the Hamiltonian, which is well justified in view of the anharmonic spectrum near the symmetry point. This leads to a Hamiltonian similar to the one from the rf-SQUID:

$$H = \mu(\Phi_{\text{ext}} - \Phi_0/2) \frac{\hat{\sigma}_z}{2} - \frac{\hbar\Delta}{2} \hat{\sigma}_x. \quad (34)$$

For this qubit, the dipole moment $\mu = 2I_p$, where I_p is the qubit persistent current in the loop (giving the name to this type of flux qubit). Δ is the energy gap that can be obtained from the numerical diagonalization of the full Hamiltonian.

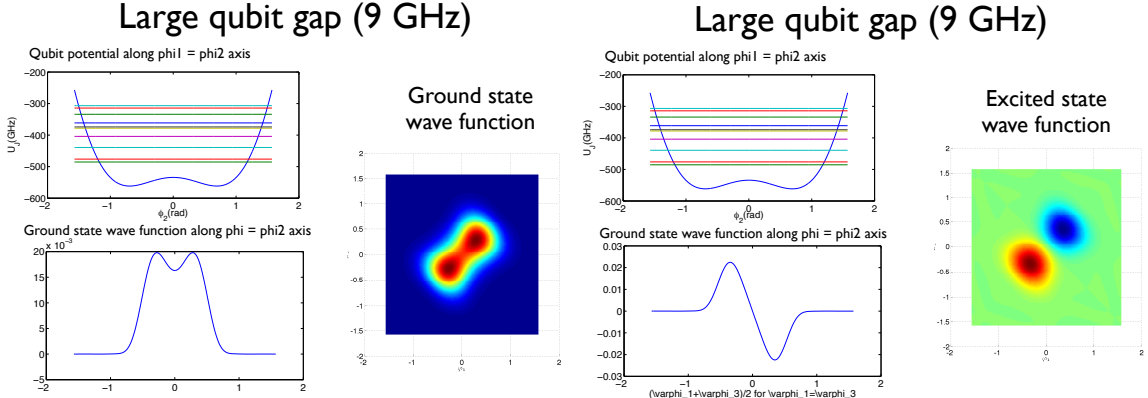


Figure 14: (Left) Flux qubit wave function in the ground state at the symmetry point for a 9 GHz gap qubit. (Right) Flux qubit wave function in the excited state at the symmetry point for a 9 GHz gap qubit.

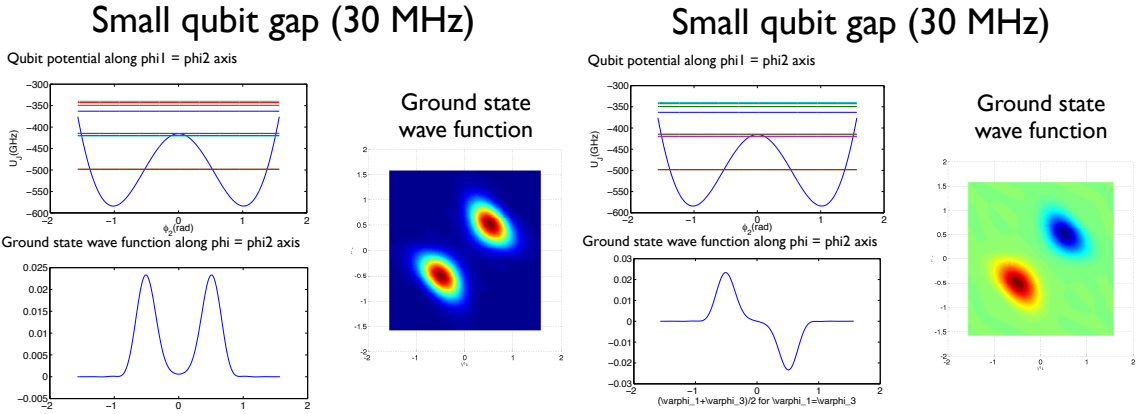


Figure 15: (Left) Flux qubit wave function in the ground state at the symmetry point for a 30 MHz gap qubit. (Right) Flux qubit wave function in the excited state at the symmetry point for a 30 MHz gap qubit.

We can implement a projective measurement of the flux qubits in the current basis, detecting the total flux trapped in the loop—i.e. the external flux plus the contribution of the qubit currents. The measurement may be performed by a dc-SQUID that is inductively coupled to the qubit. The SQUID is a sensitive magnetometer. When placed close to a flux qubit, the SQUID captures some of the qubit’s magnetic flux inside its own loop. When we apply a current to the SQUID, it will switch to a voltage state at a critical value of the current. This value depends very sensitively on the trapped flux and be used to discriminate the qubit’s state. Unfortunately, the coupling between the qubit and the SQUID is also a source of decoherence because it involves a permanent interaction between the qubit and the readout device. Nowadays, qubits are more often measured through the cavities they connect to, or using some circuit that couples or decouples the readout device, as in the D-Wave architecture. Novel techniques merging the two ideas, using a SQUID resonator, are already being implemented [30].

A combination of the flux qubit properties, large anharmonicity, large effective

magnetic dipole moment, long coherence times, have enabled this qubit to explore novel domains in quantum optics in a regime known as the ultrastrong light-matter coupling regime [31]. This is nowadays a very active area of exploration of novel fundamental physics.

3.3 Experimental implementation

The original flux qubits were designed with 2 larger junctions, and very strongly coupled to a readout DC-SQUID magnetometer. The first demonstration of spectroscopy was achieved in 2000 [28]. See Fig. 16 for a picture of the original qubit with its DC-SQUID detector. It took several years to observe coherent Rabi oscillations [32] due to a necessary re-engineering of the circuit design to not suppress qubit coherence. Then came the years in which the flux qubit was dominating the scene in terms of coherence. First, coherent oscillations of a plasma oscillation mode of the DC-SQUID readout were observed [33]. Later, in 2005, after correcting an asymmetry in the loop by adding a fourth large Josephson junction, the record of $5 \mu\text{s}$ was established for the coherence time that stood for many years [34]. Scaling the qubit circuit was pushed from early on with mutual inductive coupling [35], that later led to the first demonstration of a CNOT operation in a superconducting qubit [36]. Coherent oscillations were observed between two coupled flux qubits with high quality readout [37]. But then the flux qubit saw a stagnant period in which the group of Delft disappeared (due to the retirement of Prof. Mooij) and many groups switched to using the transmon qubit. The flux qubit had an intrinsic complication as the qubit gap at the symmetry point was unpredictable, given the exponential dependence with the junction size. Improvements were reached by turning the small qubit junction into a DC-SQUID to alleviate this complication [38, 39]. But the uncertainty remained an unsolved issue. Nevertheless, the particular properties of flux qubits, namely its large effective magnetic dipole moment, has enabled a new field of physics in light-matter interactions in the ultrastrong coupling regime, where the qubit is ultrastrongly coupled to the field of a photon in either a resonator [31], or to a propagating mode [40]. This field is exploring novel phenomena in superconducting quantum circuits that explores new physics in this unexplored domain of quantum optics, and may have an impact in the qubit technology.

It wasn't until 2016 that the MIT group made a significant leap in bringing the flux qubit back to the scene [41] by capacitively shunting the qubit (Fig. 16), in line with the transmon qubit, for better coherence and stabilization of the qubit parameters, particularly the qubit gap as now the junction capacitance is not so undefined anymore. These capacitively-shunted flux qubits achieved coherence times en-par with planar transmon qubits $T_2 \sim 40 \mu\text{s}$.

As of today, the flux qubit is still one of the most used superconducting qubits, particularly in the domain of quantum annealing, where a frustrated ground state is necessary. The Canadian-based D-Wave company has been commercializing quantum annealers made of thousands of rf-SQUID flux qubits. Despite the great engineering feat to control such a massive device, the poor quantum coherent properties

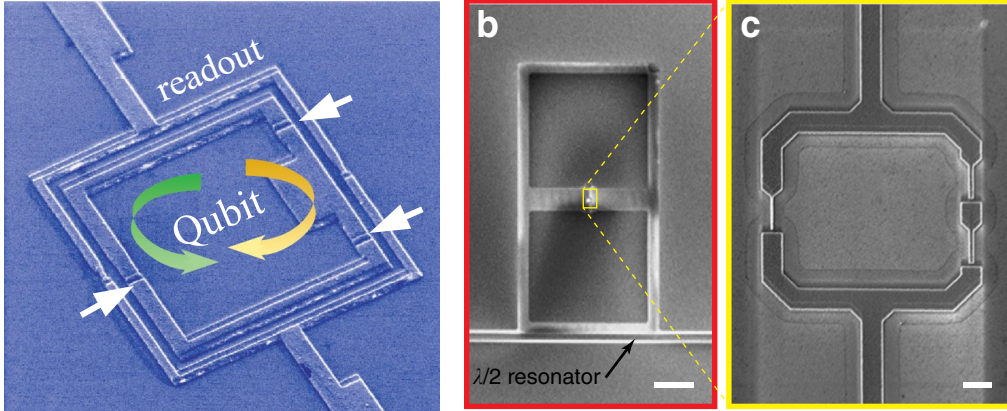


Figure 16: (Left) Old-style flux qubits read out with a DC-SQUID. From [28]. (Right) Modern, capacitively-shunted flux qubits. From [41].

of the rf-SQUIDs in D-Wave devices has led to the current state of not having attained any observable quantum advantage over classical optimization methods, particularly quantum Monte Carlo. Existing efforts in US, Europe and Japan are pushing to develop even better quantum annealers by involving high-coherence qubits. There are also efforts to build gate-based quantum computers with flux qubits, even in combination with transmon given their opposite-sign anharmonicity that leads to cancellation of spurious couplings. Therefore this qubit type is far from being out of the way, all the opposite. In fact, from a fundamental standpoint, it is one of the most interesting to study light-matter physics in combination with resonators and/or propagating modes.

4 The fluxonium qubit

The fluxonium qubit is the youngest superconducting qubit in the family, having been introduced in 2009. This qubit is both a mutation of the transmon qubit, as well as an evolved flux qubit. The fluxonium consists of a loop with a small junction, shunted by a very large inductance whose impedance at the qubit frequency far exceeds the quantum of impedance $R_Q = h/2e^2 \simeq 6.47 \text{ k}\Omega$. This so-called superinductance can be achieved by different means. In the original formulation, the fluxonium had an array of large-area Josephson junctions, acting as a linear superinductance. More recently, this junction array has been replaced by a disordered superconductor, such as granular aluminum, that exhibits very large kinetic inductance, leading to inductance values in the superinductance regime.

The fluxonium behaves as a Cooper pair box that at low frequencies has both sides of its island short-circuited, and therefore immune to charge offsets, and at large frequencies it responds like a transmon as the high impedance effectively disconnects the two junction sides. Moreover, the small critical current of the small junction limits the flux sensitivity to very low values. Altogether make the fluxonium the first qubit circuit with some intrinsic topological protection, in the way of fully topologically protected qubits, such as the π -mirror qubit or the Δ -qubit, which has recently been implemented.

Topologically, though, it is very similar to a 3-junction flux qubit, except instead of 2 larger junctions the circuit contains on the order of 100 larger ones. Contrary to the flux qubit, the fluxonium truly has a linear inductive shunt, like the rf-SQUID. Still, compared to the latter, the footprint is several times smaller, particularly the granular aluminum type.

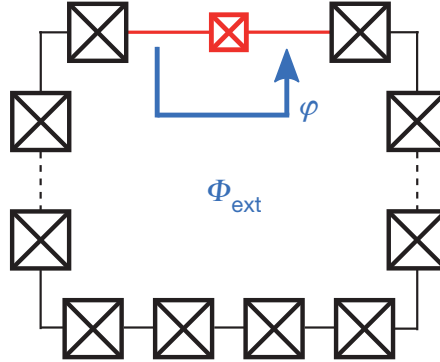


Figure 17: Fluxonium circuit schematic. From [42].

4.1 The fluxonium qubit Hamiltonian

The fluxonium Hamiltonian is that of a single junction shunted by a large linear inductor (Fig.17). Its Hamiltonian is directly

$$H = 4E_C(\hat{n} - n_g)^2 + \frac{E_L}{2} \left(\varphi^2 + 2\pi \frac{\Phi_{ext}}{\Phi_0} \right) - E_J \cos \varphi. \quad (35)$$

In presence of both a Josephson and an inductive terms, this Hamiltonian is more easily solved in the basis of phase states $|\varphi\rangle$. Here, $E_L = (\Phi_0/2\pi)^2/L$ is the inductive energy. The distinctive feature of the fluxonium is that of large inductances, meaning that it explores the regime of energies $E_L \ll E_C, E_J$. The Hamiltonian can be solved numerically to lead to the eigenstates and eigenfunctions of the fluxonium. A measured spectrum of the qubit can be seen in Fig. 18. It resembles that of a flux qubit with lower values, such that the spectrum can be fully followed down to 0 flux.

Note that in order to reach the condition $E_L \ll E_J$ implies that $L \gg \varphi_0/I_C$, which implies necessarily a superinductor given the typical parameters of qubit circuits.

4.2 Experimental implementation

The first experiments with a fluxonium qubit date from 2009, where already record T_1 times of $10 \mu\text{s}$ were attained, outperforming the best transmon and flux qubits at the time. It wasn't until 2014 (device image in Fig. 19) when an experiment of a fluxonium inside a 3D cavity showed its true potential, reaching 8 milliseconds of T_1 ! this blew the existing record by a factor 80 and is the current record of superconducting qubits. The coherence time remained comparable to the best 3D transmon,

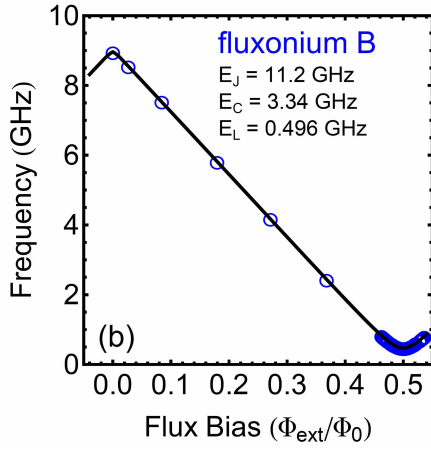


Figure 18: Fluxonium spectrum for the $0 \rightarrow 1$ transition as function of external flux. From [42].

in the tens of microsecond range. This significantly improved lifetime started to attract several groups, leading to a new record [43] with a modified fluxonium where the coherence time T_2 exceeded a millisecond, beating by a factor 10 the existing best result, set in 2012 by a 3D transmon in IBM. On top of that, many labs have begun switching from transmon to fluxonium given its improved overall coherence times, and recent 2-fluxonium qubit devices have been operated. In parallel, an alternative approach to making fluxonium qubits has been developed by the KIT group using a disordered superconductor such as granular aluminum, which displays a very high kinetic inductance, instead of the long Josephson junction array, as seen in Fig. 20. Therefore, it appears that in the long run, the fluxonium is posed to oust the transmon qubit.

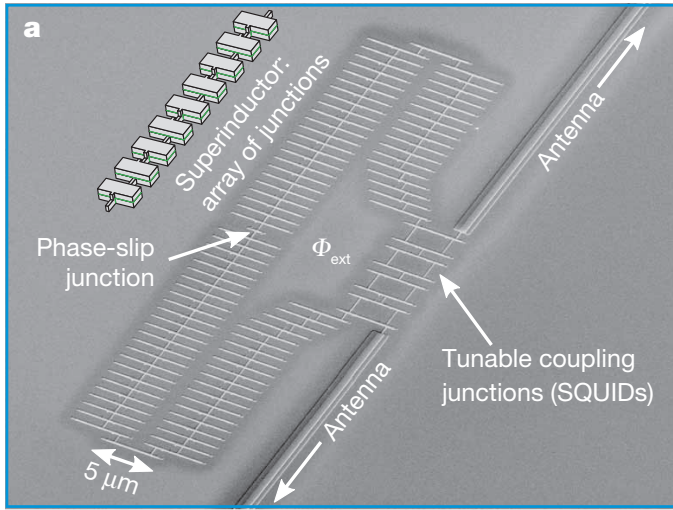


Figure 19: SEM image of a fluxonium circuit consisting of an array of Josephson junctions as a superinductance. From [42].

2-fluxonium qubit devices have not been explored until recently mainly due to the difficulty in coupling fluxoniums to each other, given their isolated nature. 2-qubit

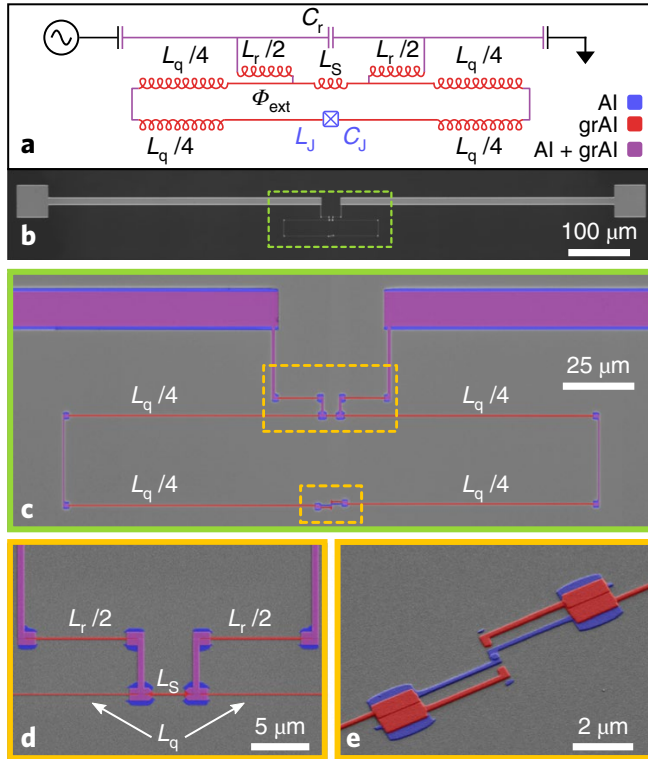


Figure 20: SEM images of a granular aluminum fluxonium-type circuit. From [44].

gates were possible eventually by involving higher-level transitions that mediated the interaction. A large-scale project led by Alibaba in China is aiming to build a fluxonium quantum computer.

5 Schrödinger Cat-State qubits

A final type of very active qubits that needs to be mentioned, without going into detail, is the Schrödinger Cat states in microwave cavities that is mainly pioneered in Yale, but also in other labs in Europe.

A harmonic oscillator on its own cannot be used as a qubit given the problem in addressing its individual quantum states using classical oscillating microwave fields. A trick to generate arbitrary states in a linear oscillator is to couple it to a qubit, that brings in nonlinearities through the qubit-cavity interaction and permits generating nonclassical states. Among these states, Schrödinger cat states have been identified as having intrinsic properties that make it a very robust qubit. An example of this type of states looks

$$|\psi_{\pm}\rangle = \frac{|+\alpha\rangle \pm |-\alpha\rangle}{\sqrt{2}}. \quad (36)$$

Being a superposition of coherent states, Schrödinger cat states do not suffer from single-photon loss, as coherent states are eigenstates of the annihilation operator, $\hat{a}|\alpha\rangle = \alpha|\alpha\rangle$. This has allowed the development of error-correcting codes at the level of a single cavity representing a logical qubit [45].

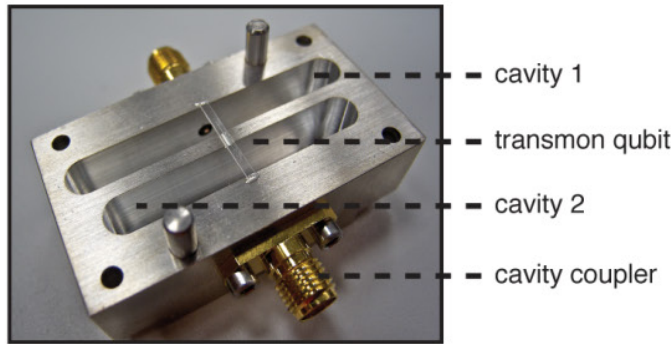


Figure 21: Optical image of a two-cavity setup with a transmon qubit joining them. One of the cavities is used to generate and store the Schrödinger cat states, the other cavity is used to read out the qubit state, which in turn is used to read out the other cavity state. From [46].

Since the qubit states live inside a microwave cavity, the quality of the states directly depends on the quality of the cavity. See Fig. 21 for images of an actual cat setup. In 3D cavities, it has been possible to reach millisecond coherence times. Even error-corrected single qubits were already demonstrated. Typically, a qubit will reside near one coupling port of the cavity so the qubit become the door to the outside world, and controls the photon emission rate into free space. This qubit does not need to be particularly coherent, easing the demands on Josephson junction technology. This qubit is used to generate Schrödinger cat states using the dynamics with the cavity mode in the dispersive regime, when the two systems do not exchange energy but exert energy shifts to one another. See Fig. 22 for state tomography of one of these cat states.

The downside of this type of qubits, and technology, is the difficulty in interacting qubits with each other, requiring a photon state to propagate along a waveguide into another cavity. This implies that any loss in the communicating channel will have an impact. Impedance mismatches, including the qubit emission/absorption of outgoing/incoming photons at the right rate. Nevertheless, the company QuantumCircuits Inc. is poised to build a quantum computer using arrays of cavities with Schrödinger cat states in them.

References

- [1] García-Ripoll, J. J. *Quantum Information and Quantum Optics with Superconducting Circuits* (Cambridge University Press, 2022).
- [2] Girvin, S. M. Superconducting qubits and circuits: Artificial atoms coupled to microwave photons (2011). Lectures delivered at Ecole d’Eté Les Houches.
- [3] Koch, J. *et al.* Charge-insensitive qubit design derived from the Cooper pair box. *Phys. Rev. A* **76**, 042319 (2007). URL <http://dx.doi.org/10.1103/physreva.76.042319>.

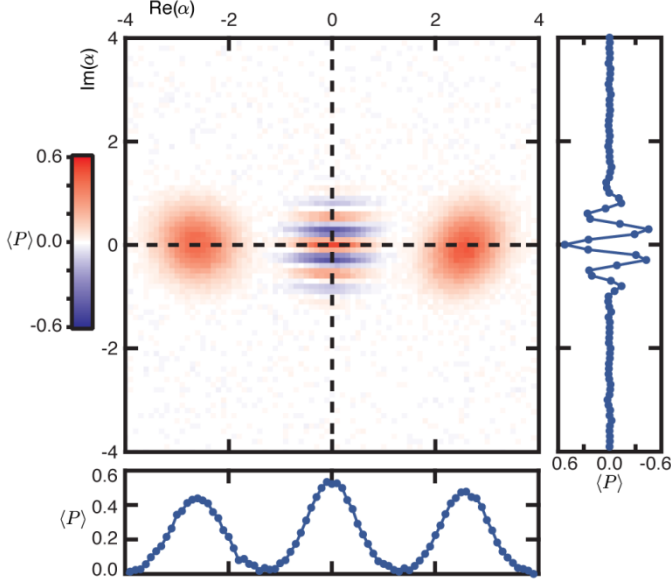


Figure 22: Tomography of a Schrödinger cat state in a 3D microwave cavity. The image shows the Wigner function of the state, displaying negative values in some phase space areas, an indication of non-classicality. The state in particular is $|\psi\rangle = (|\alpha\rangle + |-\alpha\rangle)/\sqrt{2}$. From [46].

- [4] Orlando, T. P. *et al.* Superconducting persistent-current qubit. *Physical Review B* **60**, 15398–15413 (1999). URL <http://dx.doi.org/10.1103/physrevb.60.15398>.
- [5] Nakamura, Y., Pashkin, Y. & Tsai, J. S. Coherent control of macroscopic quantum states in a single-Cooper-pair box. *Nature* **398**, 786–788 (1999). URL <http://dx.doi.org/10.1038/19718>.
- [6] Vion, D. *et al.* Manipulating the quantum state of an electrical circuit. *Science* **296**, 886–889 (2002). URL <https://www.science.org/doi/abs/10.1126/science.1069372>. <https://www.science.org/doi/pdf/10.1126/science.1069372>.
- [7] Yamamoto, T., Pashkin, Y., Astafiev, O., Nakamura, Y. & Tsai, J. S. Demonstration of conditional gate operation using superconducting charge qubits. *Nature* **425**, 941–944 (2003). URL <http://dx.doi.org/10.1038/nature02015>.
- [8] Pashkin, Y. *et al.* Quantum oscillations in two coupled charge qubits. *Nature* **421**, 823–826 (2003). URL <http://dx.doi.org/10.1038/nature01365>.
- [9] Blais, A., Huang, R. S., Wallraff, A., Girvin, S. M. & Schoelkopf, R. J. Cavity quantum electrodynamics for superconducting electrical circuits: An architecture for quantum computation. *Phys. Rev. A* **69**, 062320 (2004). URL <http://dx.doi.org/10.1103/physreva.69.062320>.

- [10] Wallraff, A. *et al.* Strong coupling of a single photon to a superconducting qubit using circuit quantum electrodynamics. *Nature* **431**, 162–167 (2004). URL <http://dx.doi.org/10.1038/nature02851>.
- [11] Astafiev, O., Yu, Nakamura, Y., Yamamoto, T. & Tsai, J. S. Quantum Noise in the Josephson Charge Qubit. *Physical Review Letters* **93**, 267007+ (2004). URL <http://dx.doi.org/10.1103/physrevlett.93.267007>.
- [12] Astafiev, O., Yu, Nakamura, Y., Yamamoto, T. & Tsai, J. S. Temperature Square Dependence of the Low Frequency $1/f$ Charge Noise in the Josephson Junction Qubits. *Physical Review Letters* **96**, 137001+ (2006). URL <http://dx.doi.org/10.1103/physrevlett.96.137001>.
- [13] Motzoi, F., Gambetta, J. M., Rebentrost, P. & Wilhelm, F. K. Simple Pulses for Elimination of Leakage in Weakly Nonlinear Qubits. *Physical Review Letters* **103**, 110501+ (2009). URL <http://dx.doi.org/10.1103/physrevlett.103.110501>.
- [14] Houck, A. A. *et al.* Controlling the Spontaneous Emission of a Superconducting Transmon Qubit. *Physical Review Letters* **101**, 080502+ (2008). URL <http://dx.doi.org/10.1103/physrevlett.101.080502>.
- [15] Majer, J. *et al.* Coupling superconducting qubits via a cavity bus. *Nature* **449**, 443–447 (2007). URL <http://dx.doi.org/10.1038/nature06184>.
- [16] Schuster, D. I. *et al.* Resolving photon number states in a superconducting circuit. *Nature* **445**, 515–518 (2007). URL <http://dx.doi.org/10.1038/nature05461>.
- [17] DiCarlo, L. *et al.* Demonstration of two-qubit algorithms with a superconducting quantum processor. *Nature* **460**, 240–244 (2009). URL <http://dx.doi.org/10.1038/nature08121>.
- [18] Fink, J. M. *et al.* Climbing the Jaynes–Cummings ladder and observing its nonlinearity in a cavity QED system. *Nature* **454**, 315–318 (2008). URL <http://dx.doi.org/10.1038/nature07112>.
- [19] Palacios-Laloy, A. *et al.* Experimental violation of a bell’s inequality in time with weak measurement. *Nature Physics* **6**, 442–447 (2010). URL <https://doi.org/10.1038/nphys1641>.
- [20] Paik, H. *et al.* Observation of high coherence in josephson junction qubits measured in a three-dimensional circuit qed architecture. *Phys. Rev. Lett.* **107**, 240501+ (2011). URL <http://prl.aps.org/abstract/PRL/v107/i24/e240501>.
- [21] Barends, R. *et al.* Coherent josephson qubit suitable for scalable quantum integrated circuits. *Phys. Rev. Lett.* **111**, 080502 (2013). URL <https://link.aps.org/doi/10.1103/PhysRevLett.111.080502>.

- [22] Barends, R. *et al.* Superconducting quantum circuits at the surface code threshold for fault tolerance. *Nature* **508**, 500–503 (2014). URL <http://www.nature.com/doifinder/10.1038/nature13171>.
- [23] Kelly, J. *et al.* State preservation by repetitive error detection in a superconducting quantum circuit. *Nature* **519**, 66–69 (2015). URL <https://doi.org/10.1038/nature14270>.
- [24] Barends, R. *et al.* Digitized adiabatic quantum computing with a superconducting circuit. *Nature* **534**, 222–226 (2016). URL <https://doi.org/10.1038/nature17658>.
- [25] Arute, F. *et al.* Quantum supremacy using a programmable superconducting processor. *Nature* **574**, 505–510 (2019). URL <https://doi.org/10.1038/s41586-019-1666-5>.
- [26] Harris, R. *et al.* Experimental investigation of an eight-qubit unit cell in a superconducting optimization processor. *Phys. Rev. B* **82**, 024511 (2010). URL <https://link.aps.org/doi/10.1103/PhysRevB.82.024511>.
- [27] Mooij, J. E. *et al.* Josephson Persistent-Current Qubit. *Science* **285**, 1036–1039 (1999). URL <http://dx.doi.org/10.1126/science.285.5430.1036>.
- [28] van der Wal, C. H. *et al.* Quantum Superposition of Macroscopic Persistent-Current States. *Science* **290**, 773–777 (2000). URL <http://dx.doi.org/10.1126/science.290.5492.773>.
- [29] Deng, C., Orgiazzi, J.-L., Shen, F., Ashhab, S. & Lupascu, A. Observation of floquet states in a strongly driven artificial atom. *Phys. Rev. Lett.* **115**, 133601 (2015). URL <https://link.aps.org/doi/10.1103/PhysRevLett.115.133601>.
- [30] Grover, J. A. *et al.* Fast, lifetime-preserving readout for high-coherence quantum annealers. *PRX Quantum* **1**, 020314 (2020). URL <https://link.aps.org/doi/10.1103/PRXQuantum.01.020314>.
- [31] Forn-Díaz, P. *et al.* Observation of the Bloch-Siegert Shift in a Qubit-Oscillator System in the Ultrastrong Coupling Regime. *Phys. Rev. Lett.* **105**, 237001 (2010). URL <http://dx.doi.org/10.1103/physrevlett.105.237001>.
- [32] Chiorescu, I., Nakamura, Y., Harmans, C. J. P. M. & Mooij, J. E. Coherent Quantum Dynamics of a Superconducting Flux Qubit. *Science* **299**, 1869–1871 (2003). URL <http://dx.doi.org/10.1126/science.1081045>.
- [33] Chiorescu, I. *et al.* Coherent dynamics of a flux qubit coupled to a harmonic oscillator. *Nature* **431**, 159–162 (2004). URL <http://dx.doi.org/10.1038/nature02831>.
- [34] Bertet, P. *et al.* Dephasing of a Superconducting Qubit Induced by Photon Noise. *Physical Review Letters* **95**, 257002+ (2005). URL <http://dx.doi.org/10.1103/physrevlett.95.257002>.

- [35] Majer, J. B., Paauw, F. G., terHaar, A. C. J., Harmans, C. J. P. M. & Mooij, J. E. Spectroscopy on Two Coupled Superconducting Flux Qubits. *Physical Review Letters* **94**, 090501 (2005). URL <http://dx.doi.org/10.1103/physrevlett.94.090501>.
- [36] Plantenberg, J. H., de Groot, P. C., Harmans, C. J. P. M. & Mooij, J. E. Demonstration of controlled-NOT quantum gates on a pair of superconducting quantum bits. *Nature* **447**, 836–839 (2007). URL <http://dx.doi.org/10.1038/nature05896>.
- [37] de Groot, P. C. *et al.* Selective darkening of degenerate transitions demonstrated with two superconducting quantum bits. *Nature Physics* **6**, 763–766 (2010). URL <http://dx.doi.org/10.1038/nphys1733>.
- [38] Paauw, F. G., Fedorov, A., Harmans, C. J. P. M. & Mooij, J. E. Tuning the Gap of a Superconducting Flux Qubit. *Phys. Rev. Lett.* **102**, 090501 (2009). URL <http://dx.doi.org/10.1103/physrevlett.102.090501>.
- [39] Fedorov, A. *et al.* Strong Coupling of a Quantum Oscillator to a Flux Qubit at Its Symmetry Point. *Phys. Rev. Lett.* **105**, 060503 (2010). URL <http://dx.doi.org/10.1103/physrevlett.105.060503>.
- [40] Forn-Díaz, P. *et al.* Ultrastrong coupling of a single artificial atom to an electromagnetic continuum in the nonperturbative regime. *Nat. Phys.* **13**, 39–43 (2017). URL <http://dx.doi.org/10.1038/nphys3905>.
- [41] Yan, F. *et al.* The flux qubit revisited to enhance coherence and reproducibility. *Nature Communications* **7**, 12964 (2016). URL <https://doi.org/10.1038/ncomms12964>.
- [42] Pop, I. M. *et al.* Coherent suppression of electromagnetic dissipation due to superconducting quasiparticles. *Nature* **508**, 369–372 (2014). URL <https://doi.org/10.1038/nature13017>.
- [43] Somoroff, A. *et al.* *arXiv:2103.08578* (2021).
- [44] Stokes, A. & Nazir, A. A master equation for strongly interacting dipoles. *New Journal of Physics* **20**, 043022 (2018). URL <http://stacks.iop.org/1367-2630/20/i=4/a=043022>.
- [45] Ofek, N. *et al.* Extending the lifetime of a quantum bit with error correction in superconducting circuits. *Nature* **536**, 441–445 (2016). URL <https://doi.org/10.1038/nature18949>.
- [46] Vlastakis, B. *et al.* Deterministically encoding quantum information using 100-photon schrödinger cat states. *Science* **342**, 607–610 (2013). URL <https://www.science.org/doi/abs/10.1126/science.1243289>. <https://www.science.org/doi/pdf/10.1126/science.1243289>.